Remote Chirality Transfer in Low-Dimensional Hybrid Metal Halide Semiconductors

Md Azimul Haque,[1] Andrew Grieder,[2] Steven P. Harvey,[1] Roman Brunecky,[1] Jiselle Y. Ye,[1,3] Bennett Addison,[1] Junxiang Zhang,[4] Yifan Dong,[1] Yi Xie,[5] Matthew P. Hautzinger,[1] Heshan Hewa Walpitage,[6] Kai Zhu,[1] Jeffrey L. Blackburn,[1] Zeev Valy Vardeny,[6] David B. Mitzi,[5,7] Joseph J. Berry,[1,4,8] Seth R. Marder,[1,4,9,10] Yuan Ping,[2] Matthew C. Beard,[1,4] Joseph M. Luther[1,4]*

[1]National Renewable Energy Laboratory, Golden, Colorado 80401, USA
[2]Department of Materials Science and Engineering, University of Wisconsin-Madison, Madison, WI, USA
[3]Department of Physics, Materials Science Program, Colorado School of Mines, Golden, Colorado 80401, USA
[4]Renewable and Sustainable Energy Institute, University of Colorado Boulder, Boulder, CO 80303, USA
[5]Thomas Lord Department of Mechanical Engineering and Materials Science, Duke University, Durham, North Carolina 27708, USA
[6]Department of Physics & Astronomy, University of Utah, Salt Lake City, UT, 84112 USA
[7]Department of Chemistry, Duke University, Durham, North Carolina 27708, USA
[8]Department of Physics, University of Colorado Boulder, Boulder, CO 80309, USA
[9]Materials Science and Engineering Program, University of Colorado Boulder, Boulder, CO 80309, USA
[10]Department of Chemical and Biological Engineering and Department of Chemistry, University of Colorado Boulder, Boulder, CO 80303, USA
*joey.luther@nrel.gov

Abstract

Chiroptical properties typically arise from structural symmetry breaking by incorporating a chiral A-site organic cation *within the hybrid metal halide structure,* limiting the compositional space. Here, we demonstrate highly efficient remote chirality transfer where chirality is imposed on an otherwise *achiral* hybrid metal halide semiconductor by a proximal chiral molecule that is not interspersed as part of the structure yet leads to large circular dichroism dissymmetry factors (g_{CD}) of up to 10^{-2}. Density functional theory calculations reveal that the transfer of stereochemical information from the chiral proximal molecule to the inorganic framework is mediated by selective interaction with divalent metal cations. Anchoring of the chiral molecule induces a centro-asymmetric distortion, which is discernible up to four inorganic layers into the metal halide lattice. This concept is broadly applicable to low-dimensional hybrid metal halides with various dimensionalities (1D and 2D) allowing independent control of the composition and degree of chirality.

Hybrid organic-inorganic metal halides exhibit pronounced chiroptical properties due to their soft, malleable lattices, heavy inorganic atoms with large spin-orbit coupling, and broadly tunable molecular components.[1] Chirality in hybrid metal halide semiconductors (MHSs) offers a new ability to manipulate charge, spin and light-matter interactions without relying on magnetic contacts or cryogenic temperatures.[2-4] Several interesting applications based upon these novel phenomena have been demonstrated, such as spin-LEDs, circularly polarized detectors, and the chiral phonon-activated spin Seebeck effect.[5-7] In MHSs, chiral organic molecules incorporated as A-site cations ensure a global chiral crystal structure and often also induce local symmetry breaking of the inorganic sub-lattice by distorting the inorganic metal-halide octahedra.[8-10] In these chiral MHSs, structural asymmetry induced by the homogeneously distributed chiral A-site enables chiroptical properties such as circular dichroism (CD), circularly polarized light emission (CPLE), and the circular photogalvanic effect (CPGE).[11,12] The current state-of-the-art for chiral MHS and associated applications are based on these structurally chiral lattices.

In addition to structurally chiral 2D MHS, promising chiroptical properties are also observed in achiral 3D MHSs, in the form of nanocrystals decorated with chiral surface ligands, metasurfaces, and chiral morphological patterning.[13-17] Chiral MHS nanocrystals are particularly interesting systems, with density functional theory (DFT) calculations suggesting that surface ligands can impart structural symmetry breaking deep into the MHS lattice without the need for the incorporation of a chiral A-site cation.[18] Taking inspiration from this phenomenon, we explored an alternative route of remotely transferring chiroptical functionality into existing achiral MHSs in a way that retains the internal composition of the achiral counterparts. Analogous to the magnetic proximity effect that has recently emerged as a powerful strategy for inducing magnetic properties into otherwise non-magnetic systems,[19] "remote chirality transfer" refers to passing on the stereochemical information from a chiral component to a proximal achiral target.[20-22] Such approaches have been recently explored for assemblies of chiral polymers and small molecules.[23,24]

Here, we demonstrate a remote chirality transfer approach, in which chirality is introduced into achiral MHS lattices via contact with a non-A-site chiral molecular additive, all while keeping the internal chemical composition of the MHS intact. We hypothesize that the presence of inhomogeneously distributed chiral entities (e.g. a gradient) in MHS thin films could provide a high degree of asymmetry with a variety of symmetry breaking mechanisms relative to structurally chiral MHSs. To test this hypothesis, we focus on BINOL (1,1′-Bi-2-naphthol) derivative chiral phosphate molecules and exploit their interactions with MHS – $(PA)_2BX_4$ (PA: Phenylammonium; B: Pb, Sn; X: I, Br). We demonstrate that the inclusion of a small amount of these non-A-site chiral molecules within MHS films induces chirality in the MHS lattice, resulting in highly tunable and significant chiroptical activity, as manifested by a large circular dichroism anisotropy factor (g_{CD}) and chiral amplification. We successfully generalize this remote chirality transfer phenomenon for various 1D and 2D MHS compositions, highlighting the versatility of this approach. An important advantage of this approach for MHSs is the potential to *independently* optimize the remote chiral and local structural components of the MHS. While chiral A-site cations provide additional chiroptical tunability to an already versatile suite of MHS optoelectronic properties, structural requirements place inevitable limits on the variety of functional chiral cations that can be incorporated directly into the MHS lattice. In contrast, a remote chirality transfer strategy could potentially transform achiral MHSs into ones that exhibit chiral behavior with chiral molecules/ligands having a much broader range of structures, functional groups, and sizes. Remote chirality transfer in hybrid metal halides also provides improved flexibility in terms of composition, spin transport properties, and complex device architectures that do not necessarily require extensive internal chemical modifications, thus enabling a new means of chiroptical tunability across the whole visible spectrum.

Results

The critical aspect we report here is that the A-site is not the only way to induce strong structural chirality in low-dimensional MHSs, as placing a large axially chiral molecule which does not incorporate into the lattice still induces widespread chiroptical character, even stronger than typical chiral A-site moieties, thus allowing additional composition and engineering controls. Such a remote chirality transfer route eliminates the need for a mandatory A-site chiral amine, as in the case of structurally chiral MHSs (Fig. 1a). In traditional terms, this is analogous to the “sergeants and soldiers effect” observed in polymers and liquid crystals,[25,26] where a small number of chiral units (in this case the chiral molecule is the sergeant) control the majority of achiral units (the MHS lattice acting as the soldiers). Motivated by solvent compatibility and the ability of different functional groups to bind to the MHS lattice, we selected the BINOL derivative phosphate group containing chiral molecules - (R)-1,1′-binaphthyl-2,2′-diyl hydrogenphosphate (*R*-BHP) and (S)-1,1′-binaphthyl-2,2′-diyl hydrogenphosphate (*S*-BHP) as the chirality inducing molecules, i.e., the sergeants. Furthermore, we hypothesize that the phosphate group in *R*/*S*-BHP can strongly bind to the uncoordinated metal cation in MHS, resulting in strong chirality transfer.

Imparting Chirality to Achiral MHS

Controlled amounts of *R*/*S*-BHP chiral molecules were introduced directly into the MHS precursor solution and simultaneously cast to achieve chiral MHS thin films. The BINOL derivative chiral molecules *R*-BHP/*S*-BHP possess axial chirality.[27,28] The large size of these chiral molecules ensures that they are not incorporated into the MHS lattice, preserving the structure and dimensionality. During crystallization, chirality is transferred from the chiral molecules to the MHS lattice (Supplementary Fig. 1). To generalize and elucidate the chirality transfer, we explored MHSs with different A-, B-, and X-site components. Since the size of the A-site spacer cation plays a significant role in determining the structural dimensionality and associated optical properties in MHSs,[29] we selected ethylammonium (EA), phenylammonium (PA), and 2-phenethylammonium (PEA) as the A-site cations to understand the impact of both aliphatic and aromatic molecules and the size of the A-site cations on the resulting dimensionalities (1D and 2D) and ultimately degree of chirality transfer. Lead (Pb) and tin (Sn) were explored as B-site components, while iodine (I) and bromine (Br) were varied on the X-site. Figure 1b shows the diffraction patterns of some representative MHSs with and without the chiral additives. The addition of chiral molecules does not significantly alter the diffraction patterns of MHSs, demonstrating the retention of the MHS structure and dimensionality with no apparent formation of new phases.

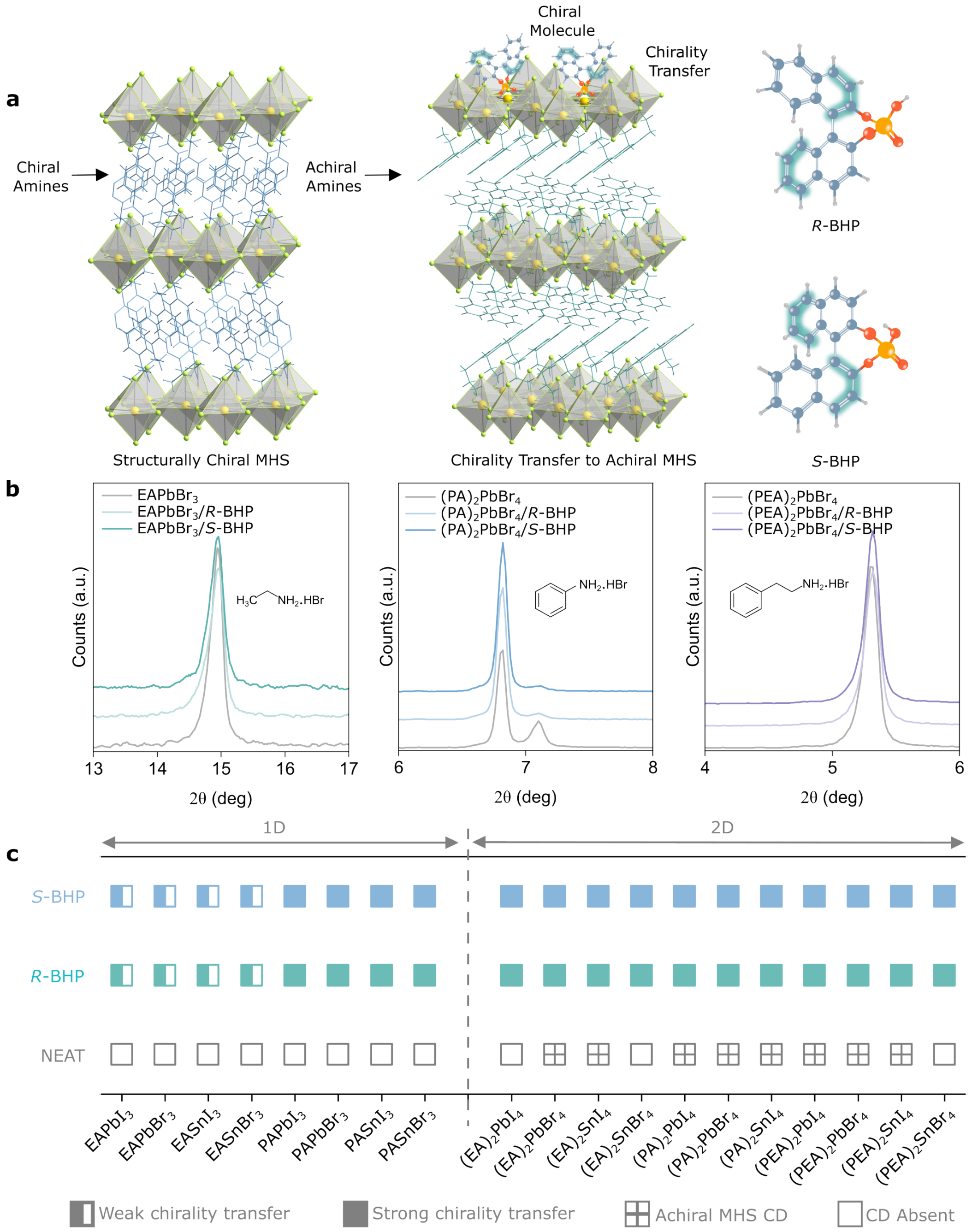

Fig. 1. Remote chirality transfer in hybrid metal halides. a, Schematic showing the difference between structurally chiral MHSs (left) and chirality transfer in achiral MHSs (middle). The molecular structure of *R*/*S*-BHP is also shown on the right. **b,** XRD pattern showing the most intense reflection for $EAPbBr_3$, $(PA)_2PbBr_4$, and $(PEA)_2PbBr_4$ remaining unchanged with or without chiral additives. The doublet peak in the case of $(PA)_2PbBr_4$ is due to the presence of a 1D phase, which is suppressed by addition of the chiral molecule. Full XRD patterns are shown in Supplementary Fig. 17. **c,** Various achiral MHS compositions (1D and 2D structures) explored in this work for chirality transfer. NEAT, *R*, and *S* represent intrinsic composition, or that with *R*-BHP and *S*-BHP chiral molecules added, respectively. Empty and crosswire squares indicate the absence and presence of a noticeable CD signal for the intrinsic composition, respectively. Half-filled and filled squares represent weak and strong chirality transfer at the band edge, respectively.

To probe the success of chirality transfer, we measured the circular dichroism (CD) and report in Fig. 1c the cases where CD is observed with opposite sign after introducing the *R*- and *S*-chiral molecules. Notably, in some cases, achiral 2D MHSs exhibit CD signatures presumably due to Rashba-Dresselhaus splitting and asymmetric disorder within the thin films.[30,31] Chirality-transfer-induced CD is fundamentally different and not simply an amplification of the CD that may occur in achiral MHSs (Supplementary Note 1, Supplementary Fig. 2-3). Unlike PEA, the EA- and PA-based MHSs can induce distinct steric effects and form different metal-halide connectivity motifs, resulting in different structural dimensionalities (1D, 2D), as a function of the precursor ratio.[32-35] Interestingly, only weak chirality transfer is observed at the band edge for the 1D MHSs based on the EA-cations despite having a similar chiral molecule distribution as that of 2D MHSs where stronger chirality transfer is observed. CD and related characterization of each composition with different precursor stoichiometries are provided in Supplementary Note 2 (Supplementary Fig. 4-16).

Chiroptical Properties of Phenylammonium-based MHS

PA-based MHSs, as reported here, are relatively rare compositions, explored mostly for passivation of solar cells and resistive switching.[36-40] We show they exhibit excellent chiroptical properties using the remote chirality transfer effect. The XRD patterns of PA-based MHSs show typical reflections of layered 2D structures (Supplementary Fig. 18). The band edge can be tuned from 400 to 600 nm as a function of the B- and X-sites for PA-based MHSs. Strong CD signals were observed for all the compositions that include *R/S*-BHP, and the CD spectral shape changed with composition, indicating the unique role of each atomic component in the structure (Fig. 2a-c). Derivative-like CD features (cotton effect) for all PA-compositions were observed around the exciton resonance similar to previously reported chiral MHSs.[41,42] The g_{CD} scaling follows the trend $(PA)_2SnI_4$ > $(PA)_2PbI_4$ > $(PA)_2PbBr_4$. Higher g_{CD} in the case of $(PA)_2SnI_4$ compared to $(PA)_2PbI_4$ agrees well with previous reports on chiral MHS where higher mixing of the chiral A-site (e.g. *R*/*S*-MBA) electronic states with Sn, compared to Pb, lead to greater symmetry breaking and therefore a higher degree of chiroptical activity.[8,43]

The optical activity can be tuned as a function of the chiral molecule concentration (Fig. 2d-f) to optimize the CD response, which is a potential advantage over the more limited tunability of structurally chiral MHSs (although chiral cation mixing also shows changes in CD with doping concentration).[44] Furthermore, an interesting but not fully understood CD inversion is observed for all PA compositions when the chiral molecule concentration crosses a certain threshold (Fig. 2d-f, Supplementary Fig. 19-21). Such CD inversion has been previously observed in MHSs and was attributed to the steric hindrance of the chiral molecules at high density.[45] In the present work, we discovered that the MHS phase controls the CD inversion. Initially, CD inversion is observed when a specific concentration of chiral molecules is reached. Subsequently, a second CD inversion occurs, restoring the CD sign, when the crystallization of the MHS phase is impeded by an excessively high concentration of chiral molecules (Supplementary Note 3, Supplementary Fig. 22-26). This CD inversion effect warrants further investigation, as it may indicate competition between different CD mechanisms and provides a unique opportunity to achieve left- or righthanded CPL absorbing/emitting MHSs from the same enantiomer.[46] The g_{CD} of $(PA)_2PbI_4$/*R*-BHP and $(PA)_2SnI_4$/*R*-BHP is significantly higher than the ubiquitously studied structurally chiral MHS $(R\text{-MBA})_2PbI_4$, underscoring the substantial chiral amplification induced by the present approach (Supplementary Fig. 27-28).

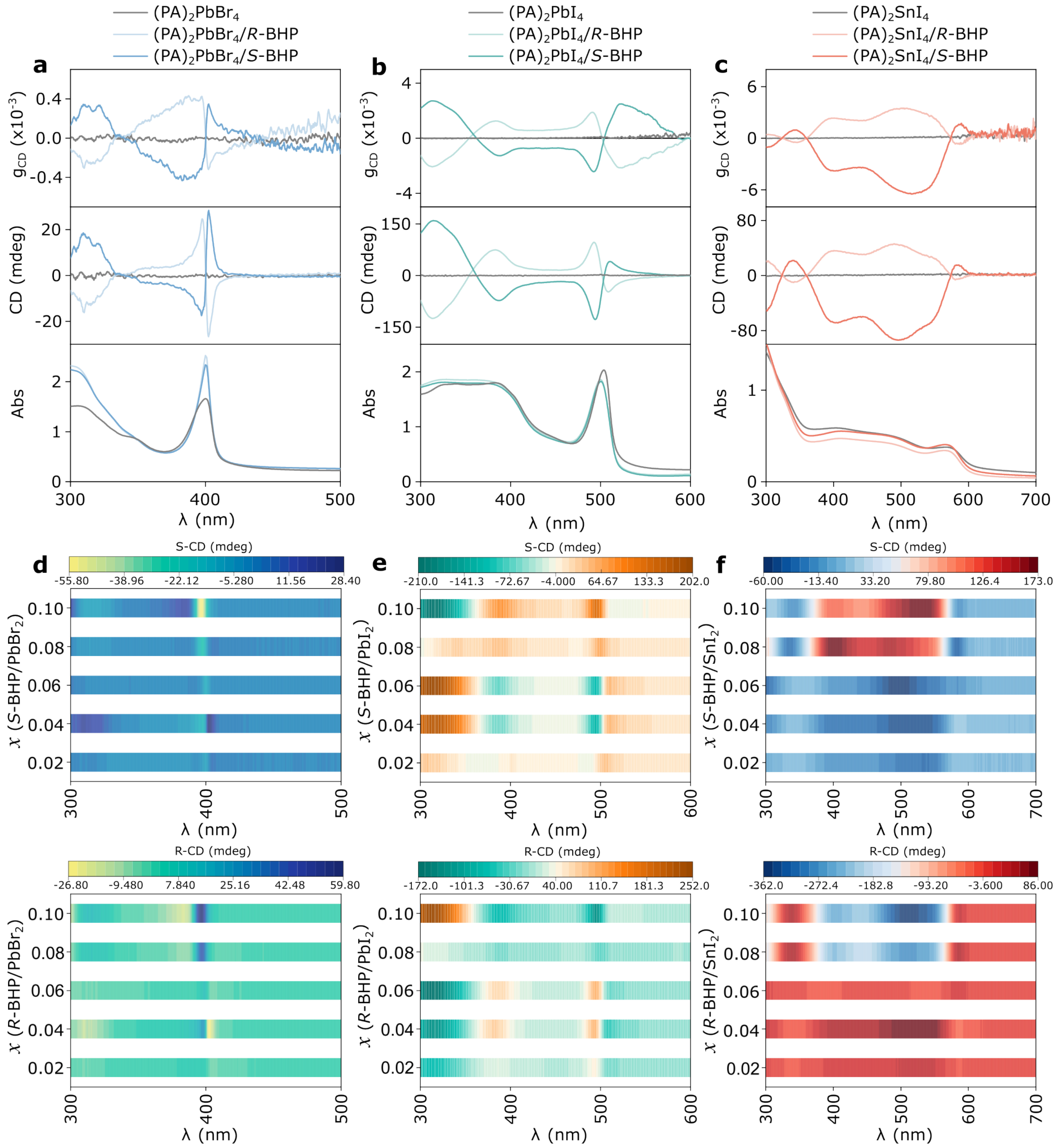

Fig. 2. Effect of composition and chiral molecule concentration on CD. a, Absorption spectra, CD, and g_{cd} for pristine and chiral MHS **a,** $(PA)_2PbBr_4$ **b,** $(PA)_2PbI_4$ **c,** $(PA)_2SnI_4$ for a 0.04 molar ratio (x) between chiral molecule and BX_2 (B: Pb, Sn; X: I, Br). The chiroptical activity can be tuned from the UV to NIR regime as a function of the B- and X-sites. 2D plots for the change in CD as a function of the chiral molecule concentration **d,** $(PA)_2PbBr_4$ **e,** $(PA)_2PbI_4$, and **f,** $(PA)_2SnI_4$. An increased concentration shows CD inversion

between the *R*- and *S*- counterparts. The critical molar ratio for CD inversion is 0.06 for $(PA)_2PbBr_4$ and $(PA)_2SnI_4$ and 0.08 for $(PA)_2PbI_4$.

Chiral Molecule Distribution and Interaction

Next, we assessed how the chiral molecule is distributed within the MHS films to create such unique functionalities. Depth-dependent elemental composition profiling by time-of-flight secondary ion mass spectrometry (TOF-SIMS) can provide insights into the incorporation and distribution of chiral molecules by monitoring the phosphorous (P) signal from the chiral molecule. Interestingly, TOF-SIMS profiles show that the molecules form a gradient throughout the film, increasing in density from the top down toward the substrate (Fig. 3a-c). The majority of the chiral molecules accumulate at the MHS-substrate interface, suggesting that the migration of the molecule during film crystallization follows a top-down crystallization process,[47,48] where the top of the film crystallizes first and expels the chiral molecules downward (Fig. 3d-f). This behavior of the chiral molecule migrating to the buried interface is substrate-independent (Supplementary Fig. 29). The chiral molecule distribution throughout the MHS film, as well as the interfacial accumulation, scales with the molecular concentration in the precursor solution (Supplementary Fig. 30-35). Notably, scanning electron microscopy (SEM) images did not show clustering of chiral molecules on the MHS film surface (Supplementary Note 4, Supplementary Fig. 36-39).

The interaction between the chiral molecule and the $(PA)_2PbI_4$ lattice was probed by solid-state NMR (ssNMR). ^{207}Pb, ^{13}C, and ^{31}P NMR measurements show strong indication that the chiral molecule interacts with Pb (Supplementary Fig. 40). 2D ^{1}H-detected ^{207}Pb – ^{1}H CP-HETCOR ssNMR of $(PA)_2PbI_4$ with and without the chiral molecule reveal numerous through-space H-Pb correlations with NH^{3+} and aromatic protons in both cases but a new, weaker correlation at ~7.6 ppm emerges only when *R*-BHP is present (Fig 3g, 3h), consistent with a through-space interaction between the *R*-BHP aromatic protons and the ^{207}Pb nuclei. The associated ^{207}Pb shift of the emerging correlation is slightly upfield relative to the bulk, as is the overall ^{207}Pb signal from the 1D ^{207}Pb solid echo (from 1125 to 1109 ppm), indicating increased shielding of the Pb nuclei. These observations suggest a through-space interaction between the chiral molecule and Pb cations. X-ray Photoelectron spectroscopy (XPS) shows a shift in the Pb 4f peak position to lower binding energy, revealing changes in the chemical bonding environment of the inorganic lattice,[49] consistent with the ssNMR results (Supplementary Fig. 41). Moreover, Fourier transform infrared spectroscopy (FTIR) exhibits deprotonation of the *R*-BHP chiral molecule and strong interaction with PbI_2 sublattice (Supplementary Note 5, Supplementary Fig. 42).

Notably, a higher concentration of chiral molecules does not necessarily result in increased chiroptical activity when comparing different PA-based MHSs. Despite $(PA)_2SnI_4$ and $(PA)_2PbI_4$ having a lower density of chiral molecules in the MHS film compared to $(PA)_2PbBr_4$ (as evidenced by TOF-SIMS), they exhibit higher g_{CD} values. However, the PA-based MHSs do exhibit a consistent compositional trend for chiroptical activity that follows Sn > Pb and I > Br, suggesting that the composition of the MHS takes precedence over the concentration of the chiral molecule in determining the degree of induced chirality.

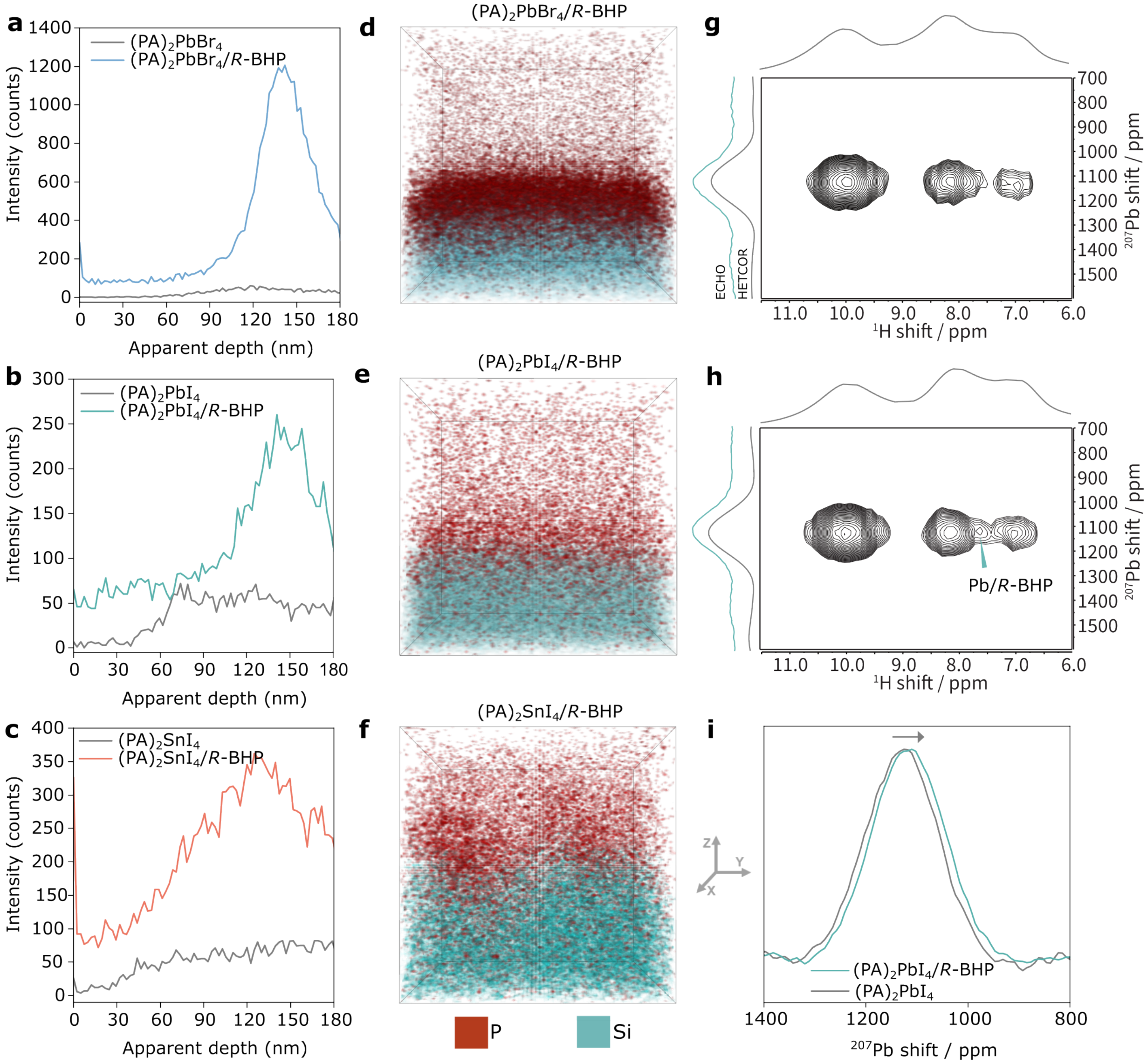

Fig. 3. Chiral molecule distribution and interaction. a-c, TOF-SIMS profiles of the P signal (corresponding to the chiral BHP molecule) for $(PA)_2PbBr_4$, $(PA)_2PbI_4$, and $(PA)_2SnI_4$ with and without chiral BHP molecules. The chiral molecules tend to aggregate at the buried interface. **d-f,** TOF-SIMS 3D rendering (25 × 25 μm) of $(PA)_2PbBr_4$, $(PA)_2PbI_4$, and $(PA)_2SnI_4$ showing P and Si signals. The distribution of the chiral molecule has a dependence on the MHS composition. Solid-state 2D $^{207}Pb(^1H)$ NMR spectra **g,** without and with **h,** the chiral molecule for $(PA)_2PbI_4$. The new feature indicated with an arrow in h appeared around 7.6 ppm due to MHS and *R*-BHP interaction. **i,** ^{207}Pb ssNMR spectra with and without the chiral molecule showing the shielding effect around the Pb-nucleus. The chiral molecule to lead halide molar ratio for all the data in Fig. 3 is 0.04.

Chirality Transfer Mechanism

To investigate the mechanism of chirality transfer and to test whether phosphate group plays a determining role as the chirality transferring entity in the case of *R*/*S*-BHP, we synthesized two chiral molecules with similar structures to those of phosphate-containing *R*/*S*-BHP but instead with methylenedioxy (*R*/*S*-BHO) and benzothia-diazole (*R*/*S*-BHS) functional groups. Across this systematic comparison, phosphate-based chiral molecules (*R*/*S*-BHP) exhibited the strongest chirality transfer for MHS $(PA)_2PbBr_4$, suggesting certain molecular design principles for chirality transfer (Fig. 4a, Supplementary Note 6, Supplementary Fig. 43-46). *R*/*S*-BHS demonstrates the importance of having the anchoring group closer to the chiral backbone. Furthermore, we establish that chirality transfer is not specific to axially chiral molecules by using a small chiral molecule methyl p-tolyl sulfoxide (*R*/*S*-MTS), which has S=O functional group (Supplementary Fig. 47). This non-axial chiral molecule transfers chirality, but with a magnitude significantly smaller than the axially chiral *R*/*S*-BHP molecule. It should be noted that the achiral BHP molecule only slightly enhances the CD signature of MHSs at the band edge (Supplementary Fig. 48).

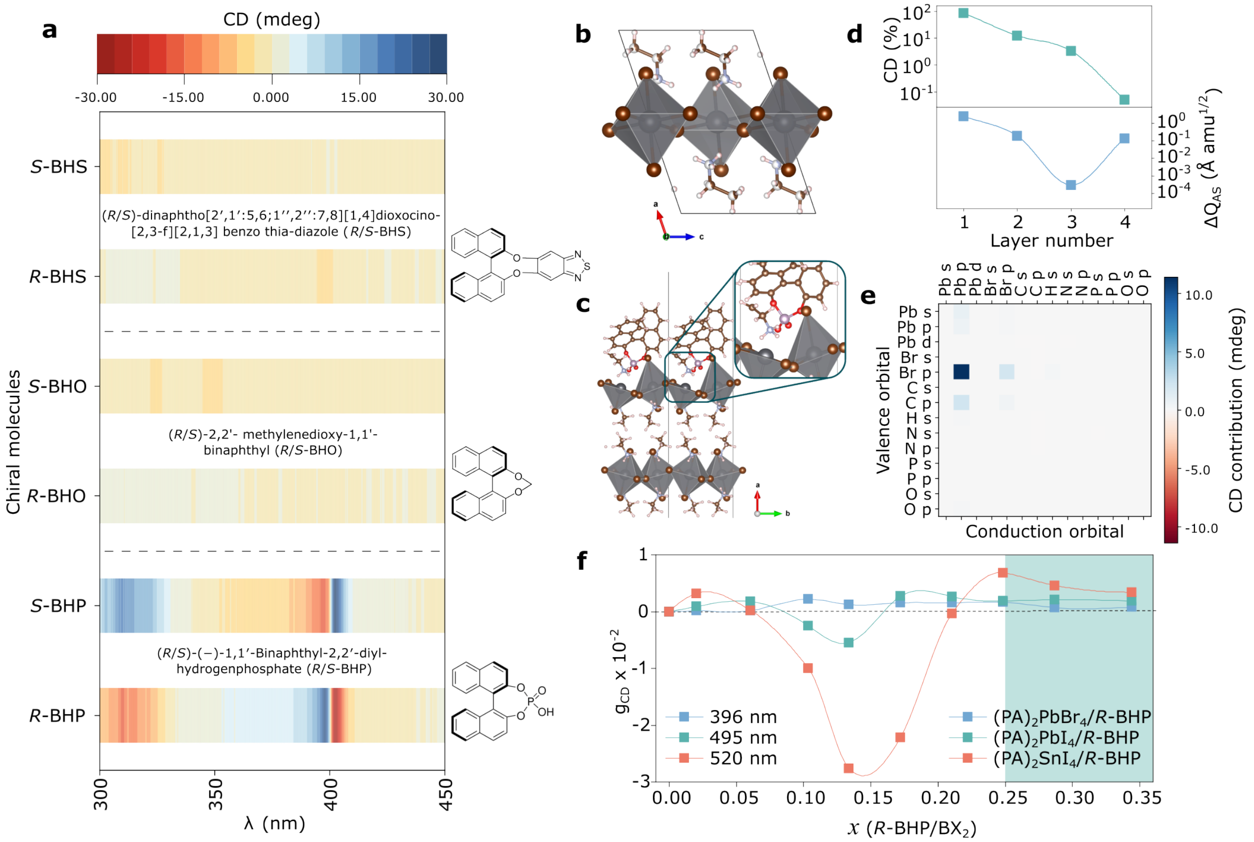

Fig. 4. Effect of the chiral molecule functional group and density functional theory calculations. a, Effect of chiral molecules with different anchoring groups on the CD of $(PA)_2PbBr_4$. *R*/*S*-BHP shows the highest degree of chirality transfer emphasizing the essential role of functional group. Atomic structure of $(EA)_2PbBr_4$ showing **b,** EA_2PbBr_4 MHS bulk **c,** EA_2PbBr_4 MHS slab with BP molecule (deprotonated BHP). **d,** Inversion-asymmetric structural distortion (ΔQ_{AS}) and contribution to CD as a function of number of inorganic layers in log scale. **e,** Orbital decomposition of CD based on transitions at 287.8 nm for BP from initial and final states in the organic molecule and inorganic lattice components. Inorganic contributions dominate the CD. **f,** Chiral amplification property of $(PA)_2PbBr_4$, $(PA)_2PbI_4$, and $(PA)_2SnI_4$, showing non-monotonic increase in g_{CD} with increasing amount of chiral molecule up to a certain concentration. The g_{CD} values in f are calculated at 396 nm, 495 nm, and 520 nm for $(PA)_2PbBr_4$, $(PA)_2PbI_4$, and $(PA)_2SnI_4$, respectively. The shaded region in f indicates the molar ratio beyond which formation of MHS phase is hindered due to high density of chiral molecules.

DFT calculations were performed to further understand the chiral molecule-MHS lattice interaction. We selected $(EA)_2PbBr_4$ (Fig. 4b) as the representative MHS for DFT simulations due to its smaller unit cell size and readily available crystallographic data.[33] $(EA)_2PbBr_4$ shows similar behavior and distribution of chiral molecules as that of PA-based MHSs (Supplementary Fig. 49). For our model, we chose the chiral molecule *R*-BHP and the deprotonated BHP molecule *R*-1-1'-binaphthyl-2,2′-diyl-phosphate (BP) to obtain insights into the chirality transfer mechanism. The possibility of *R*-BHP intercalating into the 2D MHS structure was also explored by DFT (Supplementary note 7, Supplementary Fig. 50). DFT simulations indicate that the chiral molecules do not bind to a defect-free MHS surface. Therefore, we introduced a Br vacancy at the MHS surface, motivated by the experimental evidence of chiral molecule interacting with the Pb nuclei and low halide to Pb ratios (Supplementary Fig. 51). With a Br vacancy, the chiral molecules tend to bind to the surface near the undercoordinated Pb (Fig. 4c). In this section, we focus on deprotonated chiral molecule (BP) as it binds significantly tighter to the surface (binding energy = 5.42 eV) compared to when BHP is present (binding energy = 0.92 eV), consistent with the observation of deprotonation by FTIR. The tighter binding causes the Br bond to elongate and results in significant structural distortion of the surface. The stereochemical information is transferred from the chiral molecule to the MHS lattice through this interaction. The addition of the chiral molecules introduces gap states into the band structure and projected density of states (Supplementary Fig. 52). A single gap state is introduced in the middle of the gap when *R*-BP is added. In addition to the gap states, the symmetry breaking in the inorganic bands causes splitting of the bands near the band edges. Detailed comparison of BP and BHP is provided in the supplementary information.

The degree of inversion-asymmetric structural distortion in the inorganic layer was quantified by calculating the collective structure change (ΔQ_{AS}), where $\Delta Q_{AS} = \sum_{\mathrm{i}} \Delta \boldsymbol{r}_i m_i^{1/2}$ and Δr_i^2 and m_i are the displacement (between distorted and undistorted structure) and mass of atom i, respectively of Pb and Br atoms. As expected, maximum distortion occurs in the surface layer (layer 1) with a ΔQ_{AS} of 2.48 $\text{Å}\ \boldsymbol{amu},^{\mathbf{1/2}}$ for the chiral molecule BP. While the distortion penetrates throughout the slab, lower layers (layer 2 - 4) have less distortion with similar magnitude throughout the lower layers and showing ΔQ_{AS} less than 0.24 $\text{Å}\ \boldsymbol{amu}^{\mathbf{1/2}}$ (Fig. 4d, Supplementary Table 1). The top layer has more inversion-asymmetric distortion than a chiral 2D perovskite $(S\text{-NPB})_2PbBr_4$ (NPB:1-(1-naphthyl)ethylamine) which was found to have high degree of chirality with $\Delta Q_{AS} = 2.30\ \text{Å}\ \boldsymbol{amu}^{\mathbf{1/2}}$ (referenced to an undistorted octahedron).[50]

To further understand the effect of structural distortion on chirality, CD was computed directly from DFT using electric dipole, magnetic dipole, and electric quadrupole transition matrix elements.[50] The calculated and experimental CD spectra are in good agreement beyond the excitonic peak (375-400 nm) as the current approach does not include many-body effects such as electron-hole interactions (Supplementary Note 8, Supplementary Fig. 53-54). CD predictions were decomposed into orbital contributions to elucidate the role of the organic and inorganic frameworks in the MHS structure. We find transitions from occupied Br p-orbitals to unoccupied Pb p-orbitals being the majority contributor to the CD (Fig. 4e, Supplementary Fig. 55). Transitions from occupied C p-orbitals have minor contribution to the CD and result solely from carbons located on the chiral molecule, with no contribution from the A-site molecules. This is consistent with the relationship between the structural distortion and CD contribution, where the highest contribution to CD is observed from the surface layer due to direct interaction of the inorganic layer with the chiral molecule (Supplementary Fig. 56). Apart from structural effects, electronic effects can also play a significant role in determining the CD response as in cases of chiral nanoparticles.[51-54] To separate the electronic contributions from structural distortion, we computed the CD from DFT of distorted and undistorted structures with and without chiral molecules present. We found that the combination of structural distortion and electronic effects is critical for large CD response. (Supplementary Note 9, Supplementary Fig. 57).

Discussion

This work demonstrates a new strategy for inducing chirality in achiral MHSs with high g_{CD} by introducing a chiral molecule in proximity to the inorganic lattice. The interaction between the chiral molecule and the MHS lattice induces significant lattice distortion, thereby inducing chiroptical properties. Remote chirality transfer and chiroptical tunability in the present case offer a platform for investigating chiral induction and subsequent ‘chiral amplification’ in MHSs. Chiral amplification is a unique phenomenon whereby a small chiral bias is amplified resulting in chiral assemblies with strong chiroptical properties.[55] For PA-based MHSs, the intensity of the induced CD increases non-monotonically with the number of chiral molecules, implying the occurrence of chiral amplification (Fig. 4f). Such amplification behavior provides an additional degree of freedom on stoichiometric control for designing MHS-chiral molecule assemblies with targeted interaction for high-performance chiroptical applications.[56,57] The chiroptical behavior of MHSs achieved by remote chirality transfer has almost zero linear birefringence (LB) and linear dichroism (LD) (Supplementary Fig. 58). Such LB/LD effects often mask the true chiroptical response in structurally chiral MHSs leading to observance of apparent CD and CD inversion due to optical interference.[58,59] With the available large library of 2D MHSs, our approach presents a simpler route of achieving chiral MHSs with improved performance, in contrast to structurally chiral MHSs. The high degree of circular dichroism and its dependence on chiral molecule concentration offer a promising avenue for fine-tuning chiroptical properties in MHSs. The concept of remote chirality transfer presents a unique platform for further exploration and for inducing chirality in achiral semiconductors for spintronic applications.

Acknowledgments

This work was authored in part by the National Renewable Energy Laboratory, operated by Alliance for Sustainable Energy, LLC, for the U.S. Department of Energy (DOE) under Contract No. DE-AC36-08GO28308. This project was supported by the Center for Hybrid Organic Inorganic Semiconductors for Energy (CHOISE), an Energy Frontier Research Center funded by the Office of Basic Energy Sciences, Office of Science within the U.S. Department of Energy. The views expressed in the article do not necessarily represent the views of the DOE or the U.S. Government. We thank Pattarawadee Therdkatanyuphong for providing a sample of *R*/*S*-BHO.

Author contributions

M.A.H., M.C.B., and J.M.L. conceived the idea and designed the experiments. R.B. assisted in CD measurements. S.P.H. performed the TOF-SIMS measurements. B.A. carried out the NMR experiments. M.P.H. synthesized the $(R\text{-MBA})_2PbI_4$ crystals. Y.D. and M.C.B. contributed to optical measurements. A.G.

and Y.P. performed the DFT calculations and wrote the analysis. J.Z. and S.M. synthesized the *R*/*S*-BHO and *R*/*S*-BHS chiral molecules. J.Y.Y., K.Z., and J.J.B. performed and analyzed XPS measurements. H.H.W. and Z.V.V. performed the Faraday rotation measurements. J.L.B. performed the FTIR measurements and analysis. Y.X. and D.B.M. contributed to XRD measurements and analysis. M.A.H. and J.M.L. wrote the initial draft of the manuscript, and all authors contributed to the editing of the manuscript.

Competing interests
The authors declare no competing interests.

References

1. Zhang, L., Zhang, X. & Lu, G. Intramolecular Band Alignment and Spin-Orbit Coupling in Two-Dimensional Halide Perovskites. *J. Phys. Chem. Lett.* **11**, 6982-6989, (2020).
2. Crassous, J. *et al.* Materials for chiral light control. *Nat. Rev. Mater.* **8**, 365-371, (2023).
3. Bloom, B. P., Paltiel, Y., Naaman, R. & Waldeck, D. H. Chiral Induced Spin Selectivity. *Chem. Rev.* **124**, 1950-1991, (2024).
4. Mathew, S. P., Mondal, P. C., Moshe, H., Mastai, Y. & Naaman, R. Non-magnetic organic/inorganic spin injector at room temperature. *Appl. Phys. Lett.* **105**, 242408, (2014).
5. Kim, Y.-H. *et al.* Chiral-induced spin selectivity enables a room-temperature spin light-emitting diode. *Science* **371**, 1129-1133, (2021).
6. Chen, C. *et al.* Circularly polarized light detection using chiral hybrid perovskite. *Nat. Commun.* **10**, 1927, (2019).
7. Kim, K. *et al.* Chiral-phonon-activated spin Seebeck effect. *Nat. Mater.* **22**, 322-328, (2023).
8. Lu, H. *et al.* Highly Distorted Chiral Two-Dimensional Tin Iodide Perovskites for Spin Polarized Charge Transport. *J Am Chem Soc* **142**, 13030-13040, (2020).
9. Jana, M. K. *et al.* Structural descriptor for enhanced spin-splitting in 2D hybrid perovskites. *Nat. Commun.* **12**, 4982, (2021).
10. Jana, M. K. *et al.* Organic-to-inorganic structural chirality transfer in a 2D hybrid perovskite and impact on Rashba-Dresselhaus spin-orbit coupling. *Nat. Commun.* **11**, 4699, (2020).
11. Lu, H., Vardeny, Z. V. & Beard, M. C. Control of light, spin and charge with chiral metal halide semiconductors. *Nat. Rev. Chem.* **6**, 470-485, (2022).
12. Long, G. *et al.* Chiral-perovskite optoelectronics. *Nat. Rev. Mater.* **5**, 423-439, (2020).
13. Kim, Y.-H. *et al.* Strategies to Achieve High Circularly Polarized Luminescence from Colloidal Organic–Inorganic Hybrid Perovskite Nanocrystals. *ACS Nano* **14**, 8816-8825, (2020).
14. Tran, T. K. T. *et al.* Anionic ligand-induced chirality in perovskite nanoplatelets. *Chem. Commun.* **59**, 1485-1488, (2023).
15. Long, G. *et al.* Perovskite metasurfaces with large superstructural chirality. *Nat. Commun.* **13**, 1551, (2022).
16. Kim, H. *et al.* Ultrasensitive Near-Infrared Circularly Polarized Light Detection Using 3D Perovskite Embedded with Chiral Plasmonic Nanoparticles. *Adv. Sci.* **9**, e2104598, (2022).
17. Chen, G. *et al.* Nucleation-mediated growth of chiral 3D organic-inorganic perovskite single crystals. *Nat. Chem.*, (2023).
18. Kim, Y. H. *et al.* The Structural Origin of Chiroptical Properties in Perovskite Nanocrystals with Chiral Organic Ligands. *Adv. Funct. Mater.* **32**, (2022).
19. Zhong, D. *et al.* Layer-resolved magnetic proximity effect in van der Waals heterostructures. *Nat. Nanotechnol.* **15**, 187-191, (2020).
20. Reid, J. P. Open questions on the transfer of chirality. *Commun. Chem.* **4**, 171, (2021).
21. Clayden, J., Lund, A., Vallverdú, L. & Helliwell, M. Ultra-remote stereocontrol by conformational communication of information along a carbon chain. *Nature* **431**, 966-971, (2004).
22. Zhang, Y., Wang, Y. & Dai, W.-M. Efficient Remote Axial-to-Central Chirality Transfer in Enantioselective SmI2-Mediated Reductive Coupling of Aldehydes with Crotonates of Atropisomeric 1-Naphthamides. *J. Org. Chem.* **71**, 2445-2455, (2006).
23. Ikai, T. *et al.* Control of One-Handed Helicity in Polyacetylenes: Impact of an Extremely Small Amount of Chiral Substituents. *J Am Chem Soc* **145**, 24862-24876, (2023).

24. Yashima, E. *et al.* Supramolecular Helical Systems: Helical Assemblies of Small Molecules, Foldamers, and Polymers with Chiral Amplification and Their Functions. *Chem Rev* **116**, 13752-13990, (2016).
25. Wang, Y. *et al.* Elucidation of the origin of chiral amplification in discrete molecular polyhedra. *Nat. Commun.* **9**, 488, (2018).
26. Green, M. M. *et al.* Macromolecular stereochemistry: the out-of-proportion influence of optically active comonomers on the conformational characteristics of polyisocyanates. The sergeants and soldiers experiment. *J. Am. Chem. Soc.* **111**, 6452-6454, (1989).
27. Wang, Y. B. & Tan, B. Construction of Axially Chiral Compounds via Asymmetric Organocatalysis. *Acc. Chem. Res.* **51**, 534-547, (2018).
28. Qin, T. *et al.* Atropselective syntheses of (-) and (+) rugulotrosin A utilizing point-to-axial chirality transfer. *Nat. Chem.* **7**, 234-240, (2015).
29. Mahal, E., Mandal, S. C. & Pathak, B. Understanding the role of spacer cation in 2D layered halide perovskites to achieve stable perovskite solar cells. *Mater. Adv.* **3**, 2464-2474, (2022).
30. Pham, M. T. *et al.* Strong Rashba-Dresselhaus Effect in Nonchiral 2D Ruddlesden-Popper Perovskites. *Adv. Optical Mater.* **10**, (2021).
31. Sercel, P. C., Vardeny, Z. V. & Efros, A. L. Circular dichroism in non-chiral metal halide perovskites. *Nanoscale* **12**, 18067-18078, (2020).
32. Lin, C. W. *et al.* Structure-Dependent Photoluminescence in Low-Dimensional Ethylammonium, Propylammonium, and Butylammonium Lead Iodide Perovskites. *ACS Appl. Mater. Interfaces* **12**, 5008-5016, (2020).
33. Luo, B. *et al.* Efficient Trap-Mediated Mn2+ Dopant Emission in Two Dimensional Single-Layered Perovskite (CH3CH2NH3)2PbBr4. *J. Phys. Chem. C* **123**, 14239-14245, (2019).
34. Mao, L. *et al.* Tunable White-Light Emission in Single-Cation-Templated Three-Layered 2D Perovskites (CH(3)CH(2)NH(3))(4)Pb(3)Br(10-x)Cl(x). *J. Am. Chem. Soc.* **139**, 11956-11963, (2017).
35. Ogunniran, K. O., Murugadoss, G., Thangamuthu, R., Karthikeyan, J. & Murugan, P. Integration of phenylammoniumiodide (PAI) as a surface coating molecule towards ambient stable MAPbI3 perovskite for solar cell application. *Sol. Energy Mater.* **191**, 316-328, (2019).
36. Ghoreishi, F. S. *et al.* Enhanced performance of CH3NH3PbI3 perovskite solar cells via interface modification using phenyl ammonium iodide derivatives. *J. Power Sources* **473**, (2020).
37. Kim, S. Y., Yang, J. M., Choi, E. S. & Park, N. G. Effect of interlayer spacing in layered perovskites on resistive switching memory. *Nanoscale* **11**, 14330-14338, (2019).
38. Jokar, E. *et al.* Enhanced Performance and Stability of 3D/2D Tin Perovskite Solar Cells Fabricated with a Sequential Solution Deposition. *ACS Energy Lett.* **6**, 485-492, (2021).
39. Quan, L. N. *et al.* Vibrational relaxation dynamics in layered perovskite quantum wells. *Proc. Natl. Acad. Sci.* **118**, (2021).
40. Li, Z. *et al.* A New Organic Interlayer Spacer for Stable and Efficient 2D Ruddlesden-Popper Perovskite Solar Cells. *Nano Lett.* **19**, 5237-5245, (2019).
41. Lu, H. *et al.* Spin-dependent charge transport through 2D chiral hybrid lead-iodide perovskites. *Sci. Adv.* **5**, eaay0571.
42. Long, G. *et al.* Spin control in reduced-dimensional chiral perovskites. *Nat. Photonics* **12**, 528-533, (2018).
43. Fortino, M., Mattoni, A. & Pietropaolo, A. Atomistic modeling of metal–ligand chirality transfer and chiroptical properties of lead and tin hybrid perovskites. *J. Mater. Chem. C* **11**, 9135-9143, (2023).
44. Xie, Y. *et al.* Chiral Cation Doping for Modulating Structural Symmetry of 2D Perovskites. *J. Am. Chem. Soc.* **145**, 17831-17844, (2023).
45. Wu, Y. *et al.* Ligand-Assisted Self-Assembly of 3D Perovskite Nanocrystals into Chiral Inorganic Quasi-2D Perovskites (n = 3) with Ligand-Ratio-Dependent Chirality Inversion. *Small*, e2301034, (2023).
46. Wan, L. *et al.* Inverting the Handedness of Circularly Polarized Luminescence from Light-Emitting Polymers Using Film Thickness. *ACS Nano* **13**, 8099-8105, (2019).
47. Jiang, X. *et al.* Top-Down Induced Crystallization Orientation toward Highly Efficient p-i-n Perovskite Solar Cells. *Adv. Mater.* **36**, 2313524, (2024).
48. Su, Y., Xu, C., Gao, L., Wei, G. & Ma, T. Solvent-assisted crystallization of two-dimensional Ruddlesden–Popper perovskite. *Chem. Commun.* **57**, 10552-10555, (2021).
49. Nam, J. K. *et al.* Potassium Incorporation for Enhanced Performance and Stability of Fully Inorganic Cesium Lead Halide Perovskite Solar Cells. *Nano Lett.* **17**, 2028-2033, (2017).

50. Multunas, C., Grieder, A., Xu, J., Ping, Y. & Sundararaman, R. Circular dichroism of crystals from first principles. *Phys. Rev. Mater.* **7**, 123801, (2023).
51. Jiang, W. *et al.* Emergence of complexity in hierarchically organized chiral particles. *Science* **368**, 642-648, (2020).
52. Ma, W. *et al.* Chiral Inorganic Nanostructures. *Chem. Rev.* **117**, 8041-8093, (2017).
53. Goldsmith, M.-R. *et al.* The chiroptical signature of achiral metal clusters induced by dissymmetric adsorbates. *Phys. Chem. Chem. Phys.* **8**, 63-67, (2006).
54. Noguez, C. & Garzón, I. L. Optically active metal nanoparticles. *Chem. Soc. Rev* **38**, 757-771, (2009).
55. Ishidate, R., Markvoort, A. J., Maeda, K. & Yashima, E. Unexpectedly Strong Chiral Amplification of Chiral/Achiral and Chiral/Chiral Copolymers of Biphenylylacetylenes and Further Enhancement/Inversion and Memory of the Macromolecular Helicity. *J. Am. Chem. Soc.* **141**, 7605-7614, (2019).
56. Helmich, F., Smulders, M. M., Lee, C. C., Schenning, A. P. & Meijer, E. W. Effect of stereogenic centers on the self-sorting, depolymerization, and atropisomerization kinetics of porphyrin-based aggregates. *J. Am. Chem. Soc.* **133**, 12238-12246, (2011).
57. Dressel, C., Reppe, T., Prehm, M., Brautzsch, M. & Tschierske, C. Chiral self-sorting and amplification in isotropic liquids of achiral molecules. *Nat. Chem.* **6**, 971-977, (2014).
58. Son, J. *et al.* Unraveling chirality transfer mechanism by structural isomer-derived hydrogen bonding interaction in 2D chiral perovskite. *Nat. Commun.* **14**, 3124, (2023).
59. Zhang, Z. *et al.* Revealing the Intrinsic Chiroptical Activity in Chiral Metal-Halide Semiconductors. *J. Am. Chem. Soc.* **144**, 22242-22250, (2022).
60. Sundararaman, R. *et al.* JDFTx: Software for joint density-functional theory. *SoftwareX* **6**, 278-284, (2017).
61. Giannozzi, P. *et al.* QUANTUM ESPRESSO: a modular and open-source software project for quantum simulations of materials. *J. Phys. Condens. Matter* **21**, 395502, (2009).

Methods

Chemicals and Materials

Ethylammonium iodide (EAI), ethylammonium bromide (EABr), phenylammonium iodide (PAI), phenylammonium bromide (PABr), 2-phenethylammonium iodide (PEAI), and 2-phenethylammonium bromide (PEABr) were purchased from Greatcell solar. Anhydrous DMF, SnI_2, PbI_2, *R/S*-BHP, and *R/S*-MTS were purchased from Sigma-Aldrich. $PbBr_2$ was purchased from Alfa-Aesar. *R/S*-BHO and *R/S*-BHS were synthesized as described in the Supplementary Information.

Sample preparation

PA and PEA MHS precursors were prepared by dissolving 1 M of A-cation salt and 0.5 M of metal halide salts in DMF. For 1D metal halides, 0.5 M of A-cation salt and 0.5 M of metal halide salts were mixed in DMF. For $(EA)_2BX_4$, 1.5 M of A-cation salt and 0.5 M of metal halide salts dissolved in DMF. Chiral molecules were added to the MHS precursor solution in different molar ratios to BX_2. For *R*-BHP/BX_2 molar ratios of 0.02, 0.04, 0.06, 0.08, and 0.10, the weight of *R*-BHP was 3.5 mg, 7 mg, 10.5 mg, 14 mg, and 18 mg, respectively in 1 ml of perovskite precursor. MHS films were prepared by spin-coating 50 μl precursor solution on glass substrate at 5000 rpm for 30 s, followed by annealing in a glovebox. The optimized annealing conditions are presented in Supplementary Table 2 for each composition.

Characterization

XRD measurements were performed using Rigaku Ultima IV with Cu Kα radiation at ambient temperature. SEM images were taken on a Hitachi S-4800 scanning electron microscope. UV-Vis absorption spectra were taken on a Cary 7000 spectrometer. CD measurements were carried out using a Jasco J-715 and Olis DSM 170 spectropolarimeter. An ION-TOF TOF-SIMS V spectrometer was used for depth profiling of the MHS films. XPS was performed on a Scienta-Omicron HiPP-3 system using monochromatic Al Kα X-rays (1486.6 eV), operated with a 900 μm spot size at 300W. Scans were taken with pressure between 10^{-8} and 5×10^{-8} mbar, using 200 eV pass energy and 1.5mm x 30mm entrance-slit, which approximately corresponds to 0.75eV energy resolution. Binding energy calibration was performed on silver, where Ag 3d 5/2 = 368.23 eV. Atomic percentages were calibrated using freshly cleaned polyethylene terephthalate standard. Processing of XPS data was performed using CasaXPS. The binding energy of adventitious carbon was calibrated to 285 eV. Fourier transform infrared (FTIR) absorption measurements were performed using a Thermo Scientific Nicolet iS-50 spectrometer equipped with a KBr beam splitter and a DLaGTS detector. Additional FTIR details are provided in the Supplementary Information. X-ray fluorescence (XRF) was used to determine the halide to lead ratios of the pristine MHSs films (Fischer XDV). Optical rotation and solid-state NMR measurement details are provided in Supplementary Information.

DFT calculations

The details of the DFT calculations and related methods are provided in the Supplementary Information.

Data availability

All data are available in the main article and supplementary information, or on request from the corresponding authors. Source data are provided with this paper. Supplementary Data file 1 contains the structure coordinates for lattice and relaxed ion positions.

Code availability

The codes are available through open-source software, JDFTx[60] and QUANTUM ESPRESSO,[61] or from authors upon request.